Microstructure and magnetic properties of ultrathin FePt granular films

Yuepeng Zhang,[1,a] Alan Kalitsov,[2,a] Jim Ciston,[3] Oleg Mryasov,[2] Burak Ozdol,[1] Jiangtao Zhu,[1] Shikha Jain,[1] Bing Zhang,[1] Boris Livshitz,[2] Alexander Chernyshov,[1] Antony Ajan,[1] Paul Dorsey,[1] Gerardo Bertero,[2] Ramamurthy Acharya,[1] Andrea Greene,[1] and Sharon Myers[1]

[1]*Western Digital Media, LLC, 1710 Automation Parkway, San Jose, California 95131, USA*
[2]*Western Digital Technologies, Inc., 1710 Automation Parkway, San Jose, California 95131, USA*
[3]*National Center for Electron Microscopy – Molecular Foundry, Lawrence Berkeley National Laboratory, 1 Cyclotron Road, Berkeley, California 94720, USA*

(Received 18 January 2018; accepted 20 November 2018; published online 21 December 2018)

FePt granular films with grain size smaller than 10 nm are promising candidates for storage media used in the next generation heat-assisted magnetic recording technology. However, FePt films show degraded magnetic properties when the grain size is reduced to this scale, which cannot be explained solely by the finite size theory. In this study, we explored the structural cause of property degradation by employing advanced electron microscopy and atomistic modeling. Structural features unique to the nanostructured FePt granular films at significantly reduced grain sizes of 2~8 nm were studied by high-resolution scanning transmission electron microscopy with geometric aberrations corrected up to the third order. Two critical structural parameters, the threshold grain size corresponding to the upper size limit of the FePt grains with zero chemical ordering and the sub-nanometer thin interfacial impurity at grain boundaries, were identified. A new atomistic model was developed to correlate these structural characteristics with key magnetic properties such as Curie temperature, saturation magnetization, magnetocrystalline anisotropy, and their grain-to-grain variation. The model shows good agreement with the experimental magnetic data and explains the gap in magnetic properties between the bulk and nanostructured FePt. https://doi.org/10.1063/1.5022781

Heat-Assisted Magnetic Recording (HAMR) is a novel technology promising further increase of hard disk drives (HDDs) areal density (AD). It has been claimed that to achieve 2 Tb/in^2 AD the magnetic media needs grain size reduction to less than 6 nm and tight size distribution.[1] This requires a magnetic anisotropy of the magnetic media larger than 3.5 MJ/m^3 to bypass the superparamagnetic effect that causes thermal instability of the magnetic grains when $k_BT>60K_uV$.[2] However, the current perpendicular magnetic recording (PMR) technique that uses CoCrPt layers ($K_u \sim 0.7$ MJ/m^3)[2] as storage media does not satisfy the above requirement. HAMR system, on the other hand, involving a high anisotropy granular magnetic FePt film with $K_u \sim 7$ MJ/m^3[2] as recording layer, is not subject to the above superparamagnetic constraint. In 2015 at the Intermag conference, Seagate Technology presented the first prototype HAMR HDDs, which demonstrated the feasibility of HAMR concept and FePt as storage media.[3,4] The technical difficulty of HAMR HDDs lies in recording process - the strong FePt anisotropy field prevents magnetization alignment of media bits by the conventional external writing field. In HAMR writing, a precise laser spot from near field transducer (NFT) is

[a]Corresponding Authors: YuepengZhang01@gmail.com and Alan.Kalitsov@wdc.com

firstly applied to preheat the media to a temperature near Curie temperature (T_c), when the coercivity is small. This writing process is highly sensitive to a multiple additional factors (e.g., grain-to-grain variation of Tc (σT_c) and temperature gradient of individual grains) and influences the media recording performance and the final signal-to-noise ratio (SNR) of HDDs.

In order to provide technologically relevant performance, the FePt storage film in HAMR media needs to have some specific microstructure and properties: (1) the FePt grains have an $L1_0$ ordered face-centered tetragonal (fct) structure to achieve large out-of-plane magnetic anisotropy, (2) the FePt grains are spatially isolated from each other by a non-magnetic grain boundary phase to avoid strong ferromagnetic exchange coupling between neighboring grains, (3) the size of individual FePt grains needs to be less than 6 nm to achieve 2 Tb/in^2 AD, (4) the grain-to-grain variation of magnetic properties, particularly T_c and K_u, should be small enough to guarantee lower media noise (transition jitter and DC noise), (5) the magnetic properties of FePt at extremely small grain sizes should not be significantly degraded as compared to bulk FePt.

In recent years, significant progress has been achieved in synthesizing granular FePt films with reduced grain sizes. Composite FePt nanostructures with columnar grains of less than 8 nm and non-magnetic grain boundary (GB) phase were successfully synthesized with a variety of GB materials such as Ag, BN, AlO, C, ZrO, SiO_2, TiO_2, etc.[5–20] However, there are still challenges to overcome to make HAMR drives. One of them is the relatively high media noise in HAMR drives during writing and reading, attributed to large grain-to-grain variation of magnetic properties in FePt layer.[1,21,22] It has been observed that the grain-to-grain variation of T_c (i.e., σT_c) increases rapidly with decreasing FePt grain size,[23,24] which cannot be explained solely by the finite size effect.[25] On the other hand, magnetic properties degradation of thin film FePt as compared to bulk FePt was also observed.[26,27] All these phenomena further suggest an in-depth structural and magnetic analysis of the nanostructured FePt films.

Here we studied the structural features of FePt granular films in the grain size range of 3-8 nm by high resolution Scanning Transmission Electron Microscopy (STEM) imaging with geometric aberrations corrected up to the third order and the Electron Energy Loss Spectroscopy (EELS) of 0.1 eV energy solution. A new atomistic model was developed to accommodate the identified structural characteristics to the magnetic properties. The new model explains the discrepancies in magnetic properties between the nanostructured and bulk FePt[28,29] and can be used to guide further improvement of Signal-to-Noise Ratio (SNR) of FePt-based HAMR media.

Granular FePt-X films of nominal thickness 3 nm, 4 nm, 5 nm, and 8 nm (named as S3, S4, S5, and S8 in the following text) were deposited on glass substrates by dc-sputtering in the temperature range of 450-600 °C.[7] A MgO seedlayer was deposited before the deposition of FePt to achieve [001] out-of-plane texture of FePt grains. A thin carbon film was coated on top of FePt layer as a protection layer. Structure of all samples were characterized by Transmission Electron Microscopy (TEM) and X-ray Diffraction (XRD). Magnetic properties (M_s and K_u) were measured by Physical Property Measurement System (PPMS) at room temperature.

The FePt-X films contain isolated ferromagnetic FePt grains and non-magnetic amorphous grain boundary phase X (X=Ag, C, etc.), as shown in Figure 1. The GB phase plays two important roles: (1) controls the size and shape of the FePt grains;[6] (2) decouples the magnetic exchange interaction between neighboring FePt grains. Samples S3, S4, and S5 have Ag and C as grain boundary materials. They were sputtered from the same target under the same sputtering conditions, such as Ar pressure and substrate temperature, but different sputtering time. These three samples thus have same Ag and C content and different thickness. For instance, sample S3 has shorter sputtering time and smaller film thickness, S5 has longer sputtering time and thus higher film thickness. Sample S8 was designed to have different composition from samples S3-S5. This sample contained SiO_2 segregant at grain boundary in addition to Ag and C, to demonstrate the influence of grain boundary chemistry to sample magnetic properties. We will show in the following text that sample S8 has some interface impurities at the interface between the FePt grains and the grain boundary phase. All four samples have Fe:Pt ratio of 1.

The grain size and size distribution of FePt granular grains were extracted from the plan-view TEM images (Figure 1a) and listed in Table I. Because the FePt grains have neither a regular spherical shape nor a regular cylindrical shape, but a spheroidal shape as shown in TEM plan-view and

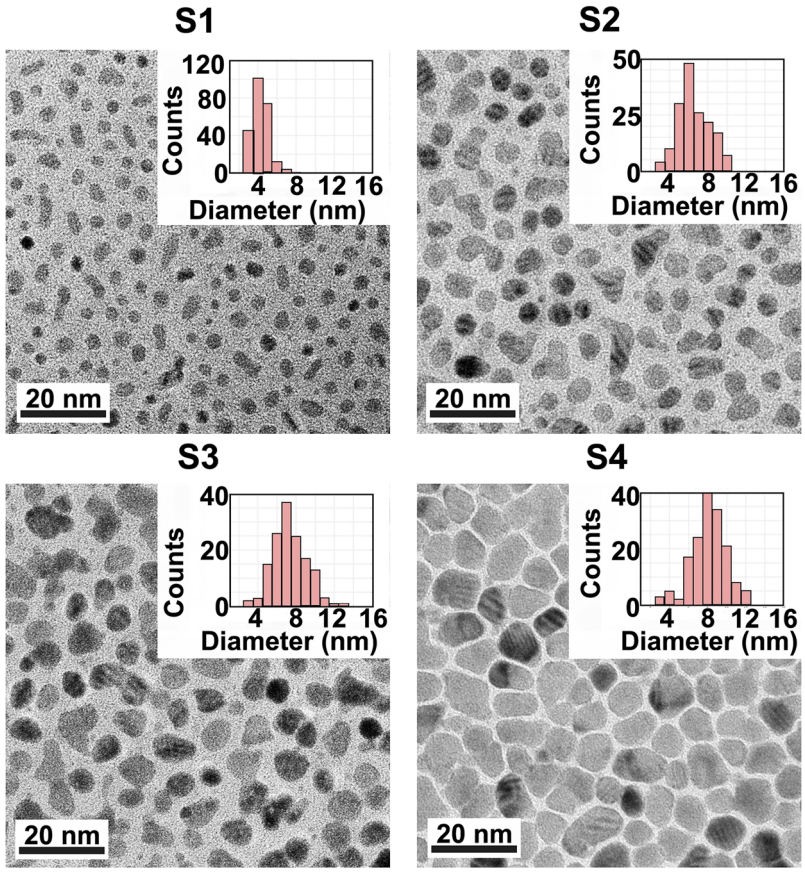

FIG. 1. TEM plan-view images of samples S3-S8, which shows the morphology of the granular FePt grains. The FePt grains show intermediate grey contrast while the grain boundary phase shows lighter contrast. The insets are the histogram of grain size (summarized in Table I).

cross-sectional images (Figure 1 and 2), in this study the grain size is defined by two parameters, i.e., grain height and grain diameter at half of the grain height. Since the grains grew throughout the FePt film thickness, the FePt grain height can be represented by the FePt film thickness. The grain diameter at half of the grain height can be extracted from the TEM plan-view images. In plan-view TEM, the electron beam passed through film thickness and project the 3D grains to a 2D image. The grain diameter shown in the plan-view image is thus the largest diameter across the entire grain height. For an ellipsoidal shaped grain, the largest diameter is the diameter at half of the height of the ellipsoid. As shown in Figure 1a, even the ellipsoidal shape of the grains are not perfectly regular. The grain diameter extracted from these images are thus calculated in three steps: (1) measure the actual area enclosed in one grain using an in-house made imaging treatment software ($A_{measured}$), (2) equalize

TABLE I. Film thickness (h), mean grain size (d), grain size distribution (σd), out-of-plane XRD measured ordering parameters (η), and in-plane XRD measured intensity ratio I_{110}/I_{220} of FePt nanostructures. The correction factors used in the (001) and (002) peak intensity evaluation are as follows. Polarization is 0.92 for (001) and 0.72 for (002), multiplicity factor is 2 for both (001) and (002), Lorenz factor is 0.33 for (001) and 0.09 for (002), absorption factor is 0.0269 for (001) and 0.0136 for (002), and temperature factor 0.9999 for (001) and 0.9996 for (002).

sample	h (nm)	d (nm)	σd (%)	η	I_{110}/I_{220}
S3	2.6	4.3	19.0	-	0.56
S4	3.6	6.5	24.6	0.67	1.30
S5	5.0	7.4	24.3	0.73	1.85
S8	8.1	8.1	22.2	0.78	1.90

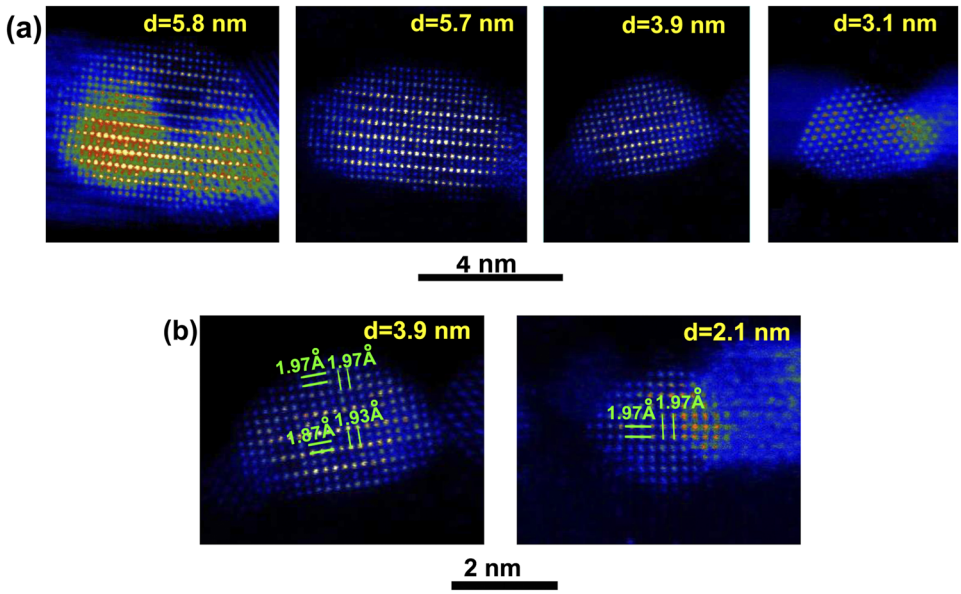

FIG. 2. (a) STEM-HAADF cross-sectional images of FePt grains of various grain sizes d, where Pt atomic columns show brighter contrast and Fe atomic columns show darker contrast, (b) d-spacing of (002) and (200) planes of FePt grains of d=3.9 nm and d=2.1 nm.

this measured area to the area of a perfectly round grain (A_{round}), (3) calculate the grain diameter (d) of the round grain and use it as an approximate grain diameter, i.e., $d = 2\sqrt{\frac{A_{round}}{\pi}} = 2\sqrt{\frac{A_{measured}}{\pi}}$. The grain size distribution was represented by the sigma of the grain size, which is $\sigma d = \sqrt{\frac{1}{N}\sum_{i=1}^{N}(d_i - d_{mean})^2}$. The chemical ordering of FePt grains, defined as $\eta = (\frac{I_{001}/I_{002}}{I_{001}^{\eta=1}/I_{002}^{\eta=1}})^{\frac{1}{2}}$ where I_{001} and I_{002} are the XRD peak intensities of the (001) superlattice plane and (002) fundamental plane, were characterized for samples S4, S5, and S8 by out-of-plane XRD (Table I, XRD raw data presented in the supplementary material) with the correction of polarization, multiplicity, Lorenz, absorption, and temperature factors[30] (see the caption of Table I). As revealed by XRD results, the FePt grains in the films are not fully ordered. The 5 and 8 nm thick FePt films in samples S5 and S8 show similar η values of 0.73 and 0.78. The 4 nm FePt film in sample S4 shows a lower η of 0.67. The ordering parameter of S3 is not quantified due to the extremely low intensities of the out-of-plane x-ray peaks of this sample. To compare the chemical ordering of this 3nm thin FePt film with other samples, grazing angle XRD was performed on samples S3-S8. The intensity ratio of the FePt superlattice (110) peak to the non-superlattice (220) peak (i.e., I_{110}/I_{220}), measured from the in-plane XRD (raw data presented in the supplementary material), was used as the criterial to evaluate the ordering. A higher I_{110}/I_{220} indicates a higher chemical ordering. It can be seen from Table I, the I_{110}/I_{220} decreases with decreasing grain size, indicating that the chemical ordering of smaller FePt grains is lower. This trend aligns with the out-of-plane XRD observation on samples S4-S8 and is also consistent with the grain size dependence of ordering reported for FePt nanoparticles prepared by wet chemistry.[31]

While the average value of the ordering parameter of each sample was obtained by XRD, how the chemical order of individual grain changes with grain size was still not clear. In order to retrieve this information, high resolution High Angle Annular Dark Field (HAADF) imaging under Scanning Transmission Electron Microscopy (STEM) mode was performed on samples S3-S5. The STEM imaging was done at National Center of Electron Microscopy (NCEM) of Molecular Foundry[32] using the TEAM 0.5 microscope at 300 kV with 17 mrad convergence angle, 68 mrad inner collection angle, and 340 mrad outer collection angle. The geometric aberrations were corrected up to the third order. The HAADF images indicate that the ordered and disordered region in an individual FePt grain at reduced grain size is not random. The larger FePt grains show disorder in the near-surface atomic planes. The volumetric fraction of the disordered region increases while the grain size decreases.

The small FePt grains only show ordering at the grain center. This trend was observed in multiple TEM specimens, in which 80-100 FePt grains per specimen were investigated. This observation is also consistent with the XRD data shown in Table I. Figure 2a shows some examples of FePt grains of sizes 5.8, 5.7, 3.9, 3.1 nm, and 2.1 nm. Note that the FePt grains have ellipsoidal shape, the grain size reported here is the grain diameter measured at the half of the grain height. The contrast in HAADF images is mainly atomic mass contrast, in which elements with higher atomic mass have bright contrast while elements with lower atomic mass show dark contrast. In Figure 2a, the bright and dark atomic columns correspond to Pt and Fe atoms, respectively. The alternation between Fe and Pt atomic columns along c-axis is a structural signature of $L1_0$ ordered FePt with [001] out-of-plane texture (i.e., the c-axis pointing to FePt film surface). As shown in Figure 2a, Fe and Pt atomic columns in the 5.7 and 5.8 nm FePt grains are alternating throughout almost the entire grain except for the first two or three surface atomic layers, indicating relatively good structural ordering. For FePt grains of size 3.9 nm, the fraction of the region that shows alternating Fe and Pt atomic layers is smaller and limited to the center of grains, suggesting a significant loss of ordering at the grain surface. When the FePt grain size is reduced to 3.1 nm, no bright versus dark contrast can be identified in the HAADF image, which means this grain is completely disordered. A careful measurement of the atomic spacing of the disordered 3.1 nm FePt grain indicates that this grain has a cubic crystal structure instead of tetragonal structure. This observation suggests that the loss of ordering in FePt is accompanied by a crystal structure change. To further confirm this observation, we measured the d-spacing of two orthogonal planes (200) and (002) of the partially ordered grain of 3.9 nm grain size. This grain indeed shows equal d-spacing of (200) and (002) planes at the surface disordered region but different value at the ordered region in grain center, as shown in Figure 2b. Consistently, an even smaller FePt grain of 2.1 nm grain size shows completely loss of ordering and has cubic structure (Figure 2b). Note that in this study of disorder, a total of 6 samples were evaluated by TEM, with between 80 and 100 grains measured per sample. Across all measurements (approximately 500 grains in total), ~80 grains below 3.1 nm in size showed a complete loss of ordering. The remaining ~420 grains with sizes above 3.1 nm all showed some degree of ordering. It should also be mentioned that the $L1_0$ ordering formation and the value of d_η depends on the fabrication parameters, such as deposition temperature, post-deposition annealing temperature, and annealing time.

The microscopy observation suggests some important information. At very small grain size (e.g., < 5nm) FePt grains have low ordering. The loss of ordering in individual FePt grains is associated with crystal structure change from tetragonal to cubic. When grain size is reduced, the surface of FePt grains loses chemical ordering first. The fraction of the disordered region increases with decreasing grain size until a threshold grain (d_η) size is reached, below which the FePt grains are fully disordered and have cubic structure. The presence of d_η in our FePt granular film is consistent with earlier experimental data of FePt nanoparticles prepared by wet chemistry,[31] and was attributed to particle size effect associated with nanostructured FePt, such as the decrease of order-disorder transition temperature with grain size, the surface effect, and the composition fluctuation in nanoparticles.[33] The incomplete ordering of FePt grains has a large impact on grains magnetic properties, in particular Curie temperature and magnetic anisotropy. This influence will be discussed in details with the assistant of atomistic modeling in the following text.

Besides crystal structure and ordering, the effect of interface impurity on the magnetic properties was also studied, for the reason that such effect is common and significant for nanomaterials with heterogeneous microstructure like a grain boundary phase. The interface impurity was found on FePt films (sample S8) with SiO_2 grain boundary phase. The Electron Energy Loss Spectroscopy (EELS) study of this sample shows a thin iron-oxide shell on the surface of FePt grains. The presence and nature of the oxide shell was investigated. The EELS study was done under STEM mode at both 80 and 300 kV: single EELS spectrum used for phase identification was done at 80 kV with a 30 mrad convergence angle, a 38 mrad collection angle, a Zero Loss Peak (ZLP) of 0.1 eV FWHM, EELS line scan was conducted at 300 kV to achieve good spatial resolution of 0.15nm while keep 0.2 eV FWHM of ZLP, where the convergence and collection angle is set as 17 mrad and 25.5 mrad, respectively. Figure 3a shows the HAADF image of S8, from which the EELS spectra were collected. Figure 3b contains the intensity profiles referenced to the HAADF to visually identify the SiO_2 grain boundary (GB) region and the FePt-SiO_2 interface. High intensity in Figure 3b corresponds to the

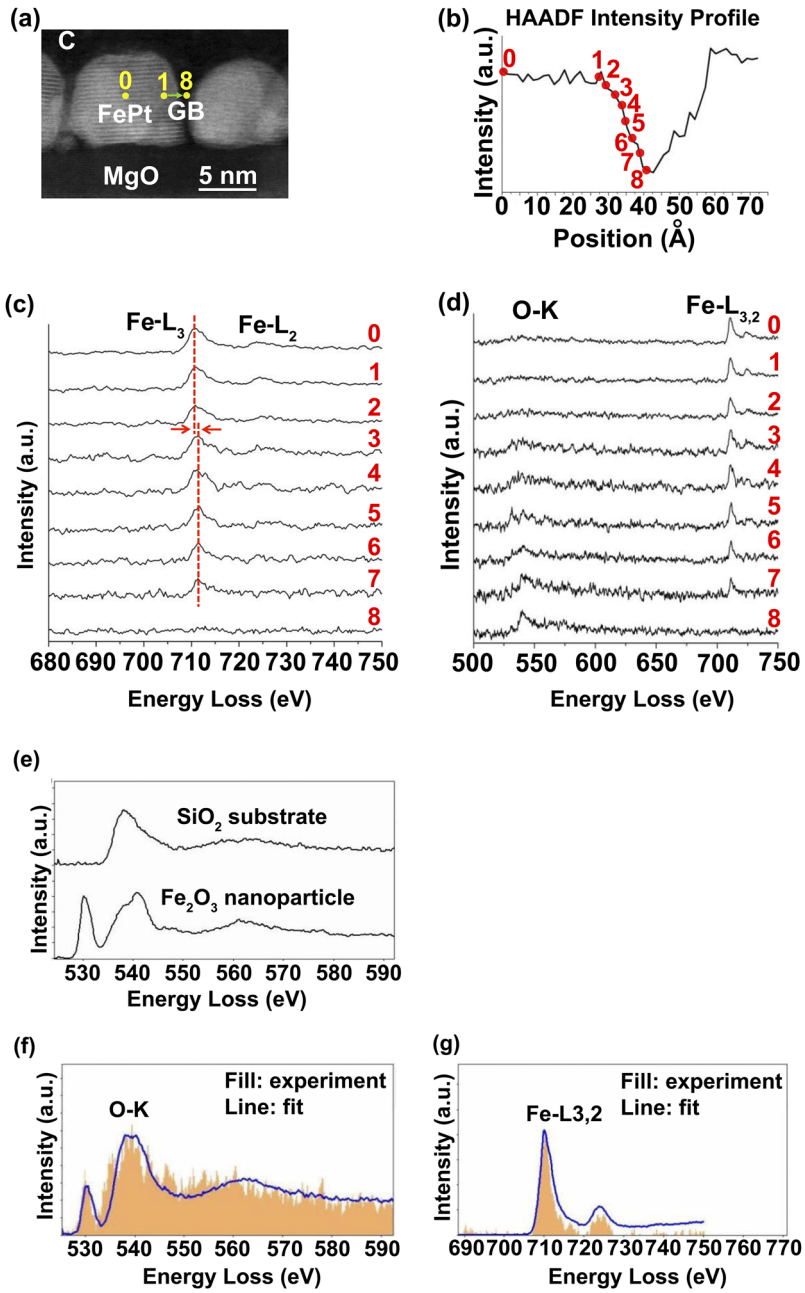

FIG. 3. (a) STEM-HAADF of FePt grains in sample S8, where the EELS line scan was taken, (b) Intensity profile of the HAADF image taken simultaneously with EELS line scan. Center of the FePt grain (spot "0") and the line scan positions at the FePt-GB interface (spots "1"-"8") are labeled, (c) EELS spectra collected in the energy range of Fe-L_{23} edge (680-750 eV) at spot "0" and line 1-8, (d) EELS spectra collected in the energy range of both O-K and Fe-L_{23} edge (500-750 eV) at spot "0" and line 1-8, (e) EELS spectra of reference SiO_2 and Fe_2O_3 nanoparticles, (f) MLLS fitting of the O-K and (g) Fe-L23 edge of the oxide shell by reference spectra of SiO_2 and Fe_2O_3 shown in (e).

bright region in Figure 3a. EELS spectra were collected at the center of FePt grain (spot "0") and across FePt-SiO_2 interface through a line scan (line "1-8" in Figures 3a, b) with a step size of 0.15 nm. Immediately noticed from the EELS spectra in Figure 3c is a single Fe L-edge at energy onset of 709 eV of spectrum #0, which is consistent with the metallic nature of FePt. Also noticeable is a single peak at the energy onset of ~534 eV of spectrum #8, which corresponds to the oxygen K-edge of the SiO_2 GB phase. However, the most important information comes from spectra 1-7, as

these spectra were collected across the FePt-SiO_2 interface. Spectra #2 and #3, which only show Fe L-edge, are similar to spectrum #1 indicating that these two spectra are from pure FePt. For spectra #3-7, an oxygen K-edge is shown together with a Fe L-edge, indicating the FePt-SiO_2 interface. A close comparison of the oxygen edge of spectra #3-7 with spectrum #8 reveals that the oxygen edge of spectra #3-7 contains a small pre-edge at ~530 eV, which is absent in spectrum #8. This pre-edge peak is a signature of iron-oxide with Fe^{3+} ions[34] and indicates that Fe oxidation with Fe^{3+} oxidation state forms at the FePt-SiO_2 interface. Concurrently, a 0.8 eV shift of Fe L3 edge towards the high loss region is observed in spectra #3-7, as compared to spectrum #1-3 (Figure 3d). The energy shift, often accompanying the change of chemical state of Fe, is another sign of iron-oxide formation.[34] A quantitative estimation of the Fe and O content of the iron-oxide showed higher O:Fe ratio of 6.8 than that of Fe_2O_3 (=1.5), possibly due to the capture of oxygen signal from SiO_2 GB phase at the vicinity of the FePt-SiO_2 interface. Note that the electron beam transmits through the sample thickness, and thus may capture EELS signal of the GB phase on top of or below the FePt grains. To confirm this assumption, spectra of FePt-SiO_2 interface region, SiO_2 boundary phase, and Fe_2O_3 reference nanoparticles were collected under the same experimental conditions. The FePt-SiO_2 interface spectrum was well fit by the combining the reference spectra of SiO_2 and Fe_2O_3 using Multiple Linear Least-Square (MLLS) fitting, as shown in Figure 3e–g.

The surface oxidation of the FePt grains suggests a core-shell structure containing an FePt core and Fe oxidation shell with Fe^{3+} oxidation state. The shell thickness, estimated from EELS line scan steps between #3 and #7 (with a step size of 0.15 nm), is about 0.4 nm, with the consideration of EELS delocalization of 0.2 nm for oxygen K-edge and Fe L-edge under 300 kV.[35]

The above TEM observations suggest two structural features unique to the nanostructured FePt. One is the threshold grain size d_η, the other is the weakly- or non-magnetic interface impurity of thickness Δ. A good evaluation of the magnetic performance of the FePt nanostrucutres should include these structure factors. In this study, we developed a new atomistic model that serves this purpose. The new model introduces the phenomenological parameters d_η and Δ to a previously developed atomistic model for bulk FePt,[36] and parameterizes the magnetic entities as expressions of grain size (d) and grain size dependent order parameter $\eta(d)$. Such parameterization simplifies the magnetic calculation of FePt nanostructures, since all the magnetic properties become a function of grain size. The average properties of FePt nanostructures are obtained with known grain size distribution that was obtained from TEM study.

The first step in terms of building the new model was to make atomistic Monte Carlo simulations of magnetic properties on finite size FePt grains. The shape of the grains was assumed to be cylindrical for simplification. The effective Hamiltonian of magnetic interactions in FePt was parameterized by first principle calculations.[36] The parametric expressions were fit by numerical data measured by experiments to obtain critical exponents and critical diameters.

The diameter dependence of order parameter was parameterized by Monte Carlo study for the 3D Ising model,[37]

$$\eta(d,h) = \eta^{\infty}(h)\left(1 - \left(\frac{d_\eta}{d}\right)^{\gamma_\eta}\right)$$

where $\eta^{\infty}(h) = \eta(h, d \to \infty)$ is the order parameter of a thin film with thickness h and scaling exponent $\gamma_\eta = 2.6$. The critical diameter d_η is the grain diameter below which the grain becomes completely disordered. The critical diameter value may vary from grain to grain. However to simplify our analyses we fixed d_η to one value for all grains.

The Curie temperature diameter dependence follows the finite size scaling law,[25]

$$T_C(d,h,\eta) = \left(T_C^{L10}(h) - 150\left(1 - \frac{\eta(d)}{\eta^{\infty}(h)}\right)\right)\left(1 - \left(\frac{d_0}{d}\right)^{\gamma_{T_C}}\right)$$

where d_0 is the critical diameter that determines the minimum magnetic grain size, and γ_{T_C} is the corresponding scaling exponent.[23,25] The factor $T_C^{L10}(h) - 150\left(1 - \frac{\eta(d)}{\eta^{\infty}(h)}\right)$ accounts for the ordering effect of the Curie temperature. This factor reflects that the Curie temperature of a completely disordered FePt grain is 150 K lower than thin $L1_0$ FePt film.[31]

The temperature dependence of the magnetization is parameterized with the following expression,

$$f_m(d,h,\eta,T,T_C) \equiv \frac{M_s(d,h,\eta,T,T_C)}{M_s(d,h,\eta,T=0)} = \left(1 - s\left(\frac{T}{T_C(d,h,\eta)}\right)^{\frac{3}{2}} - (1-s)\left(\frac{T}{T_C(d,h,\eta)}\right)^{p}\right)^{1/3}$$

where the weight parameter $s = 3.02$ and the power parameter $p = 2$ represent a good fit to the numerical data.

The magnetic anisotropy parameterization is given by,

$$K_1(d,h,\eta,T,T_C) = K_1^{L10}(T=0,h)\left(1 - \left(\frac{d_K}{d}\right)^{\gamma_K}\right)\left(\frac{\eta(d,h)}{\eta^{\infty}(h)}\right)^2 f_K(d,h,\eta,T,T_C)$$

where factor $\left(1 - \left(\frac{d_K}{d}\right)^{\gamma_K}\right)$ accounts for the reduction of FePt anisotropy in small grains due to finite size effect even at $T = 0$ K. This size dependence of magnetic anisotropy at zero temperature can be understood in the framework of FePt anisotropy model.[36] According to this model the Pt-induced spin moments result in additional isotropic and anisotropic contributions that in turn depend on the average number of atomic neighbors. For a FePt thin film, the number of neighbors of an atom at the surface of grain is less than that for a bulk FePt due to symmetry breakup. Therefore, the anisotropic contribution induced by Pt moments also depends on grain size.[38] The factor $f_K(d,h,\eta,T,T_C) = f_m^{\gamma_K}(d,h,\eta,T,T_C)$ corresponds to the temperature dependent scaling of the uniaxial anisotropy with respect to magnetization.[36]

With the aforementioned steps, the magnetic properties of a single grain with size d are obtained, which can be used to get the average properties of FePt nanostructures. For example, the average Curie temperature and its standard deviation are given by

$$\langle T_C \rangle = \int \partial d f(d) T_C(d,h,\eta(d))$$

$$\sigma T_C = \sqrt{\int \partial d f(d)(T_C(d,h,\eta(d)) - \langle T_C \rangle)^2}$$

In our analysis we assumed that the distribution function $f(d)$ is a Gaussian distribution with average diameter $\langle d \rangle$ and standard deviation σ_d, measured from TEM.

The effect of interface impurity at the FePt-GB interface can be taken into account in the framework of a non-magnetic shell model. A FePt grain of height h, diameter d, and non-magnetic shell of thickness Δ can be viewed as the reduction of the magnetic diameter of a FePt grain by 2Δ. The effect of shell on the order parameter is expected to be small and neglected in our analyses. However the shell significantly influences the Curie temperature due to finite size effect. The presence of shell also reduces the saturation magnetization because of the reduction of the magnetic volume. The magnetic anisotropy is affected through both the reduction of magnetic volume and the drop of the Curie temperature.

$$T_C(d,h,\eta,\Delta) = \left(T_C^{L10}(h) - 150\left(1 - \frac{\eta(d)}{\eta^{\infty}(h)}\right)\right)\left(1 - \left(\frac{d_0}{d-2\Delta}\right)^{\gamma_{T_C}}\right)$$

$$M_s(d,h,\eta,\Delta,T,T_C) = M_s(d,h,\eta,\Delta=0,T=0)\left(\frac{d-2\Delta}{d}\right)^2 f_m(d,h,\eta,T,T_C)$$

$$K_1(d,h,\eta,\Delta,T,T_C) = K_1(d,h,\eta,\Delta=0,T=0)\left(\frac{d-2\Delta}{d}\right)^2 f_K(d,h,\eta,T,T_C)$$

Here, the factor $\frac{V_m}{V} = \left(\frac{d-2\Delta}{d}\right)^2$ corresponds to the reduction of the magnetic volume of the FePt grain caused by the presence of a non-magnetic shell.

The calculated magnetic properties of samples S5 and S8 are summarized in Table II. Samples S3 and S4 are not considered for magnetic evaluation, low film thickness caused noise in PPMS data. In comparison of the measured and calculated magnetic parameters of samples S5 and S8, our model shows good agreement with experimental trend. The model predicts well the anisotropy

TABLE II. Saturation magnetization (Ms) and magnetic anisotropy (Ku) of samples S5 and S8 (measured vs. calculated).

	M_s (emu/cm^3)			K_u (MJ/m^3)		
sample	measured	calculated	calculated[a]	measured	calculated	calculated[a]
S5	980	875	-	4.2	4.2	-
S8	800	726	892	3.4	3.4	4.9

[a]Structural phenomenological factors not included in calculation.

constant K_u, but shows a lower M_s for both samples. Considering that there exists a large FePt grain size distribution, we believe the difference in the calculated and measured M_s is introduced by inaccuracy in the estimation of magnetic volume in FePt-X films. Taken into account that samples S5 and S8 have different microstructure, i.e., thickness, grain size, with and without oxide shell, the same trend in calculation and measurements indicates that the model is robust. To demonstrate the advantage of the new model, calculation of the magnetic properties where the microstructural factors are not included is also presented in Table II. It can be seen that the new model predicts the magnetic properties much more precisely. Here we would like to point out that the newer more sophisticated model does not add any additional fitting parameters since the phenomenological parameters such as shell thickness, ordering parameters, threshold grain size, can all be determined directly from experiments.

Figure 4 plots the model prediction of T_c, σT_c, M_s, and K_u as a function of threshold grain size d_η and oxide shell thickness of FePt nanostructures having a similar microstructure to sample S8. It is clear that T_c and σT_c are more sensitive to d_η than Δ. As shown in Figure 4a, at a certain d_η value, T_c drops 6 K when Δ increases from 0 to 0.5 nm. However, the change of T_c reaches 30 K when d_η changes from 0 to 4 nm at Δ=0.5 nm. Similar strong dependence on d_η was seen for σT_c. As shown in Figure 4b, σT_c doubles when d_η increases from 0 to 4 nm at Δ=0.5 nm. Unlike T_c, M_s is affected mainly by Δ. As shown in Figure 4c, M_s shows a large vertical change over Δ range but relatively flat curves over d_η range. In terms of K_u, both d_η and Δ play a strong role, as illustrated in Figure 4d. These simulation results clearly demonstrate the strong impact of the structural factors on the intrinsic magnetic properties of nanostructured FePt. As shown in Figure 4, in comparison with a defect free FePt film (d_η=0, Δ=0), the degradation of magnetic properties of the core-shell FePt

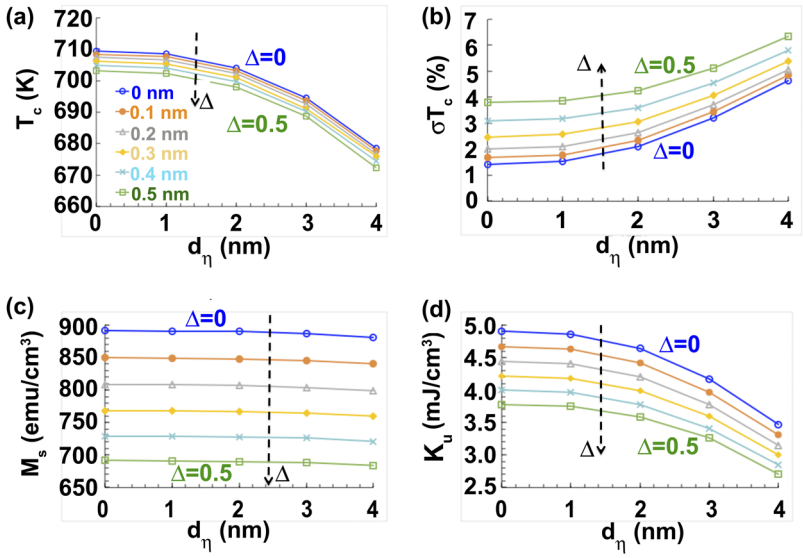

FIG. 4. Magnetic properties calculated for FePt nanostructures with similar dimensions of sample S8 with various shell thicknesses (Δ = 0~0.5 nm) and threshold grain size (d_η). (a) T_c temperature, (b) σT_c, (c) M_s, (d) K_u. The legend of b-d is the same as a. The black dotted line shows the trend of small to large Δ.

granular nanostructures studied here (i.e., 0.4 nm thickness shell and a threshold grain size d_η=3 nm) is quite pronounced: 31% drop in K_u, 19% reduction in M_s, 3% decrease in T_c, and two times increase in σT_c.

In summary, the present study identified critical structure characteristics associated with FePt granular nanostructures. The $L1_0$ ordering decreases gradually with decreasing grain size until a threshold grain size is reached, where the entire grain changes to disordered cubic structure. For the incompletely ordered FePt grains, the core of the grain always has good ordering while the near surface region is disordered. Regarding heterogeneous FePt-X system with a non-magnetic X grain boundary phase, the impurity at the FePt-X interface also changes the overall magnetic behavior of the system. An atomistic model that incorporates the microstructure characteristics was developed, which shows more precisely evaluation of the magnetic properties of nanostructured FePt. Our modeling results indicate that the Curie temperature and its grain-to-grain variation are strong functions of the order parameter, while the saturation magnetization is affected mainly by the interface impurity. The anisotropy constant, on the other hand, is strongly influenced by both structure factors. These observations can guide further improvement of FePt-based HAMR magnetic media.

See supplementary material for

A. In-plane and out-of-plane M(H) loops of samples S5 and S8 measured at room temperature.
B. In-plane and out-of-plane XRD profiles of the samples S3-S8.

Work at the Molecular Foundry was supported by the Office of Science, Office of Basic Energy Sciences, of the U.S. Department of Energy under Contract No. DE-AC02-05CH11231.

NOMENCLATURE

HAMR	heat-assisted magnetic recording
AD	areal density
HDD	hard disk drive
PMR	perpendicular magnetic recording
NFT	near field transducer
GB	grain boundary
PPMS	Physical Property Measurement System
STEM	Scanning Transmission Electron Microscopy
HAADF	High Angle Annular Dark Field
EELS	Electron Energy Loss Spectroscopy
ZLP	Zero Loss Peak

[1] D. Weller, G. Parker, O. Mosendz, E. Champion, B. Stipe, X. Wang, T. Klemmer, G. Ju, and A. Ajan, IEEE Trans. Magn. **50**, 3100108 (2014).
[2] D. Weller, O. Mosendz, G. Parker, S. Pisana, and T. S. Santos, Phys. Status Solidi A **210**, 1245–1260 (2013).
[3] Seagate HAMR Demo at InterMag 2015 conference, http://blog.seagate.com/business/seagate-demos-hamr-drives-at-intermag-conference/.
[4] C. Rea, P. Subedi, H. Zhou, D. Saunders, M. Cordle, P. Lu, S. Granz, P. J. Czoschke, S. Hernandez, J. Jury, Y. Peng, J. Thiele, A. Q. Wu, G. Ju, T. Rausch, M. Seigler, and E. Gage, TMRC 2016, Invited Presentation – A1, Stanford, USA, 2016.
[5] B. S. D. Ch. S. Varaprasad, M. Chen, Y. K. Takahashi, and K. Hono, IEEE Trans. Magn. **49**, 718–722 (2013).
[6] B. S. D. Ch. S. Varaprasad, J. Wang, T. Shiroyama, Y. K. Takahashi, and K. Hono, IEEE Trans. Magn. **51**, 3200904 (2015).
[7] H. Yuan, A. Chernyshov, J. Mardinly, K. Srinivasan, R. Acharya, G. Bertero, and T. Yamashita, J Appl. Phys. **109**, 07B772 (2011).
[8] H. Pandey, J. Wang, T. Shiroyama, B. S. D. Ch. S. Varaprasad, H. Sepehri-Amin, Y. K. Takahashi, A. Perumal, and K. Hono, IEEE Trans. Magn. **52**, 3200108 (2015).
[9] Y. Shao, M. L. Yan, and D. J. Sellmyer, J. Appl. Phys. **93**, 8152–8154 (2003).
[10] S.-C. Chen, P. C. Kuo, A. C. Sun, C. T. Lie, and W. C. Hsu, Mater. Sci. Eng. B **88**, 91–97 (2002).
[11] J. A. Christodoulides, P. Farber, M. Daniil, H. Okumura, G. C. Hadjipanayis, V. Skumryev, A. Simopoulos, and D. Weller, IEEE Trans. Magn. **37**, 1292–1294 (2001).
[12] D. H. Ping, M. Ohnuma, K. Hono, M. Watanabe, T. Iwasa, and T. Masumoto, J. Appl. Phys. **90**, 4708–4716 (2001).
[13] M. Daniil, P. A. Farber, H. Okumura, G. C. Hadjipanayis, and D. Weller, J. Magn. Magn. Mater. **246**, 297–302 (2002).
[14] M. Watanabe, T. Masumoto, D. H. Ping, and K. Hono, Appl. Phys. Lett. **76**, 3971–3973 (2000).
[15] T. O. Seki, Y. K. Takahashi, and K. Hono, J. Appl. Phys. **103**, 023910 (2008).
[16] O. Mosendz, S. Pisana, J. W. Reiner, B. Stipe, and D. Weller, J. Appl. Phys. **111**, 07B729 (2012).

[17] T. Shiroyama, T. Abe, Y. K. Takahashi, and K. Hono, IEEE Trans. Magn. **49**, 3616–3619 (2013).
[18] E. Yang and D. E. Laughlin, J. Appl. Phys. **104**, 023904 (2008).
[19] H. Ho, E. Yang, D. E. Laughlin, and J.-G. Zhu, Appl. Phys. Lett. **102**, 112411 (2013).
[20] Y. F. Ding, J. S. Chen, B. C. Lim, J. F. Hu, B. Liu, and G. Ju, Appl. Phys. Lett. **93**, 032506 (2008).
[21] R. Acharya, TMRC 2014, Invited Presentation – D3, Berkeley, California, USA, 2014.
[22] J.-G. Zhu and H. Li, J. Appl. Phys. **115**, 17B747 (2014).
[23] A. Lyberatos, D. Weller, G. J. Parker, and B. C. Stipe, J. Appl. Phys. **112**, 113915 (2012).
[24] A. Chernyshov, T. Le, B. Livshitz, O. Mryasov, C. Miller, R. Acharya, and D. Treves, J. Appl. Phys. **117**, 17D111 (2015).
[25] O. Hovorka, S. Devos, Q. Coopman, W. J. Fan, C. J. Aas, R. F. L. Evans, X. Chen, G. Ju, and R. W. Chantrell, Appl. Phys. Lett. **101**, 052406 (2012).
[26] S. Pisana, O. Mosendz, G. J. Parker, J. W. Reiner, T. S. Santos, A. T. McCallum, H. J. Richter, and D. J. Weller, Appl. Phys. **113**, 043910 (2013).
[27] S. Wicht, V. Neu, L. Schultz, D. Weller, O. Mosendz, G. Parker, S. Pisana, and B. Rellinghaus, J. Appl. Phys. **114**, 063906 (2013).
[28] O. A. Ivanov, L. V. Solina, V. A. Denshina, and L. M. Magat, Phys. Met. Metallogr. **35**, 81 (1973).
[29] K. Watanabe and H. Masumoto, Trans. Jpn. Inst. Met. **9**, 627 (1983).
[30] E. Yang, D. E. Laughlin, and J. Zhu, IEEE Trans. Magn. **48**, 7–12 (2012).
[31] C. Rong, D. Li, V. Nandwana, N. Poudyal, Y. Ding, Z. L. Wang, H. Zeng, and J. P. Liu, Adv. Mat. **18**, 2984–2988 (2006).
[32] National Center of Electron Microscopy (NCEM) - Molecular Foundry, http://foundry.lbl.gov/facilities/ncem/.
[33] R. V. Chepulskii and W. H. Butler, Phys. Rev. B **72**, 134205 (2005).
[34] L. A. J. Garvie and P. R. Buseck, Nature **396**, 667–670 (1998).
[35] R. F. Egerton, *Electron energy loss spectroscopy in the transmission electron microscope*, 2nd Edition (Plenum Press, New York, 1996).
[36] O. N. Mryasov, U. Nowak, K. Y. Guslienko, and R. W. Chantrell, Europhys. Lett. **69**, 805 (2005).
[37] M. M. Tsypin and H. W. J. Blöte, Phys. Rev. E **62**, 73 (2000).
[38] A. Lyberatos, D. Weller, and G. J. Parker, J. Appl. Phys. **114**, 233904 (2013).